WAVE SPEED MEASUREMENTS IN NON-IDEAL COMPRESSIBLE FLOWS USING THE FLEXIBLE ASYMMETRIC SHOCK TUBE (FAST)

T. Mathijssen [1], M. Gallo [1], E. Casati [1], A. Guardone [2], P. Colonna [1*]

[1] Propulsion & Power, Delft University of Technology
2629 HS, Delft, The Netherlands
P.Colonna@tudelft.nl

[2] Department of Aerospace Science & Technology, Politecnico di Milano
Via La Masa 34, Milano 20156, Italy

* Corresponding Author

ABSTRACT

Non-ideal compressible fluid dynamics (NICFD) are defined as compressible fluid flows occurring in the dense vapour, dense vapour-liquid equilibrium or supercritical thermodynamic region. This type of flow can occur in expanders of organic Rankine cycle power plants. In order to study NICFD, a Ludwieg tube-type facility has been designed and constructed at Delft University of Technology. A large variety of fluids can be employed in the facility, but for this study D_6 siloxane is chosen as working fluid due to its high thermal stability and the possibility of encountering non-classical gasdynamic phenomena. This compound belongs to the siloxane class, which are also used as working fluids in ORC power systems. Gasdynamic experiments within the NICFD region are presented from which the wave speed and speed of sound can be inferred using the time-of-flight technique. These data can be used to improve and validate thermodynamic models.

1. INTRODUCTION

The field of fluid mechanics studying the motion of fluids in the dense-vapour, dense-vapour-liquid and supercritical thermodynamic region is called Non-ideal compressible fluid dynamics (NICFD). Such flows are characterized by, among other interesting phenomena, a quite different variation of the sound speed compared to that of ideal gases. This feature can be investigated by considering the fundamental derivative of gasdynamics Γ, defined by Thompson (1971) as

$$\Gamma \equiv 1 + \frac{\rho}{c}\left(\frac{\partial c}{\partial \rho}\right)_s, \tag{1}$$

in which ρ, c and s denote the fluid density, speed of sound, and entropy respectively. For an ideal gas, Γ is constant and equal to $(\gamma + 1)/2$ in ideal gases, in which γ is the ratio of specific heats. Whenever Γ is variable among the thermodynamic states of the fluid flow, NICFD occurs (Thompson, 1988).

The working-fluid flows within turbomachinery of Organic Rankine Cycle (ORC) power systems is one example where NICFD is encountered (Cramer, 1989; Brown and Argrow, 2000; Colonna et al., 2015). Other examples encompass supercritical carbon dioxide ($scCO_2$) power systems (Conboy et al., 2012; Rinaldi et al., 2015) and high temperature heat pumps (Zamfirescu and Dincer, 2009).

Flow measurements in the dense vapour region of complex organic fluids can contribute to the improvement of thermodynamic models and to the understanding of NICFD. ORC turbine designs benefit from better thermodynamic models through a more accurate prediction of flow patterns, such as shock waves. However, measurements in dense vapours of high molecular weight fluids are scarce (Nannan et al.,

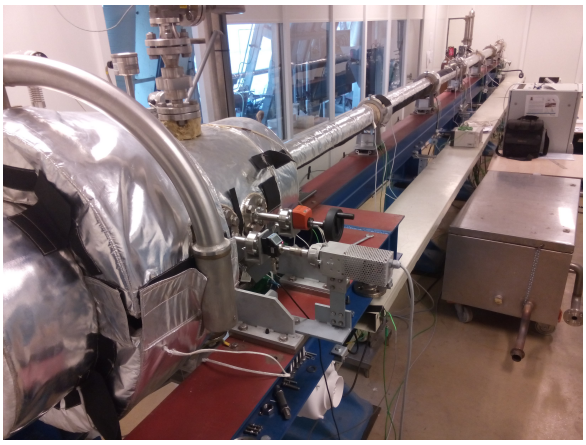

Figure 1: Picture of the FAST setup. In the foreground the LPP is visible, with the charge tube extending to the other side of the room. The vapour generator and condenser are not visible in this image.

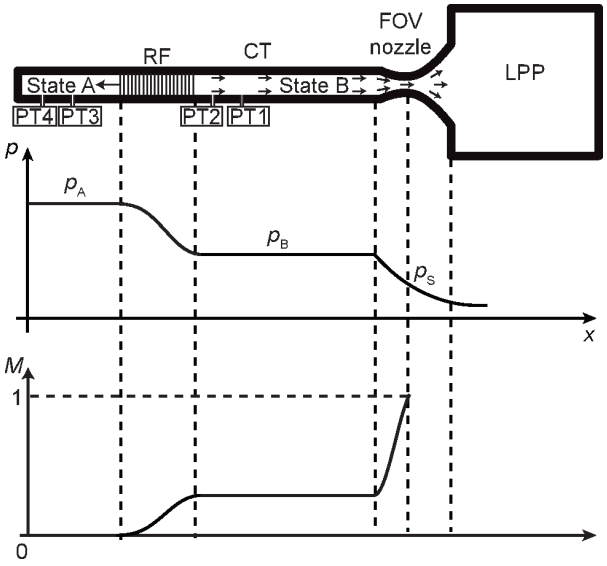

Figure 2: Schematic overview of a rarefaction wave experiment after opening the FOV. A rarefaction fan (RF) propagates into the charge tube (CT) at sonic speed W. The rarefaction starts a flow from stagnant condition A in the CT to condition B. It flows through a choked nozzle to the low pressure plenum (LPP). The pressure p and Mach number M along the tube are displayed qualitatively.

2007; Weith et al., 2014). In order to fill this gap, the flexible asymmetric shock tube (FAST), an unconventional Ludwieg tube, is designed and installed at Delft University of Technology (Colonna et al., 2008a), in the Netherlands, with the aim of studying wave propagation in the dense vapour of organic compounds.

This work documents the FAST set-up and the first experimental results of wave propagation measurements in the dense vapour of dodecamethylcyclohexasiloxane (D_6). Fig. 2 shows a schematic overview of a classical rarefaction wave experiment. The charge tube (CT) is filled with the dense organic vapour and kept at the desired pressure and temperature. The fast-opening valve (FOV), initially closed, is opened, thus allowing the fluid to flow towards the low pressure plenum (LPP), which is maintained at a lower pressure. Consequently a rarefaction travels into the CT.

A description of the set-up is provided in Sec. 2: it provides details about the components equipping the complete system as-built, the experimental procedure, and an overview of the control and data acquisition system. The results of the rarefaction wave experiments in a variety of incondensable gases are reported and discussed in Sec. 3. In Sec. 4 results from preliminary rarefaction wave measurements in D_6 are reported. Sec. 5 summarizes concluding remarks and outlines future work.

2. THE FAST AND THE EXPERIMENTAL PROCEDURE

The mechanical and heating equipment is described in Sec. 2.1 by outlining the procedure of a typical experiment. The measurement and monitoring instruments as well as the control system are briefly reported in Sec. 2.2.

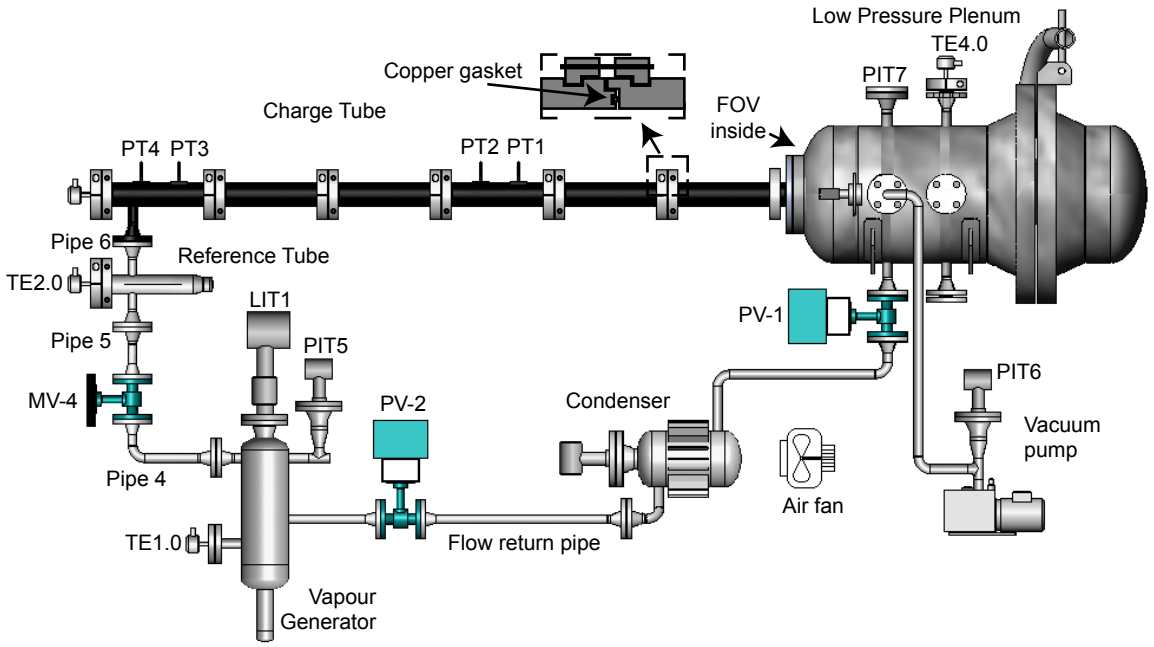

Figure 3: Overview of the FAST setup. Relevant labels are placed to the equipment and instruments. The fast-opening valve is placed inside the low pressure plenum.

2.1 Equipment & procedure

A schematic representation of the FAST is reported in Fig. 3. All pipes, vessels, and parts in contact with the working fluid are made of stainless steel (316Ti).

Before starting an experiment the working fluid needs to be purified in order to remove air and moisture deemed as the main causes of thermal decomposition of the adopted organic compounds at high temperature (Dvornic, 2004). The fluid, after being filtered with a 3Å molecular sieve and a paper filter, is inserted into a stainless steel Swagelok cylinder (type 304L-HDF-81CAL) and a Pfeiffer vacuum pump (type Duo 5 M) is used to extract any incondensable gases. By immersing the cylinder in a pool of liquid nitrogen, the fluid freezes and, as a consequence, releases the dissolved gases that are extracted by using a vacuum pump once the fluid has melted. This freezing-thawning procedure is repeated at least 2 times before filling the vapour generator through pipe 1, see Fig. 4.

The vapour generator is a custom made 5.9 liter vessel, designed to heat and evaporate the working fluid isochorically (valves MV-4 and PV-2 closed, see Fig. 3) up to the desired pressure and temperature by utilizing electric heaters. Most of the thermal energy is supplied to the vapour generator by a 1.5 kW Kurval ceramic band heater (custom built ETB HRHK-type) covering the bottom section, see Fig. 4, because the lower part of the vapour generator is always in contact with liquid. This ensures a high heat transfer coefficient between the heater and the liquid fluid inside the vessel and helps avoiding hot spots that could trigger thermal decomposition of the fluid. Preliminary tests revealed periodic instabilities of the thermal control induced by condensation phenomena occurring in the unheated section of the vessel (pipe 2 and 3, Fig. 4). By heating all the walls of the vapour generator, these instabilities were eliminated. Therefore, the main section of the vessel is heated by a 2.8 kW ceramic band heater (custom built ETB HRHK-type). The complex geometry of the top section made the implementation of a band heater impossible, so the upper section of the vapour generator is heated with a 6 m long 1 kW Welvy Joule dissipation heating wire (type HSQ/060). Another heating wire of the same type is wrapped around pipe 2 and 3, and a third wire around pipe 4, see Fig. 3. Where possible to apply, the heating element presses into a KWX 2 mm conducting graphite layer (type KU-CBGA2000-0H) to improve the thermal contact, which also ensures an even surface temperature distribution, thanks to its high in-plane thermal

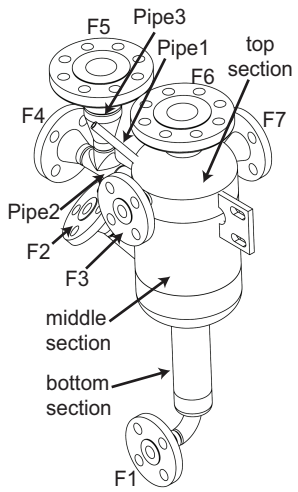

Figure 4: Drawing of the vapour generator. The numbers correspond to the flanges connecting with the following equipment: F1: outlet to extract liquid, F2: PT-100 sensor, F3: return pipe from the LPP, F4: burst disc, F5: static pressure transducer, F6: liquid level meter, F7: reference tube

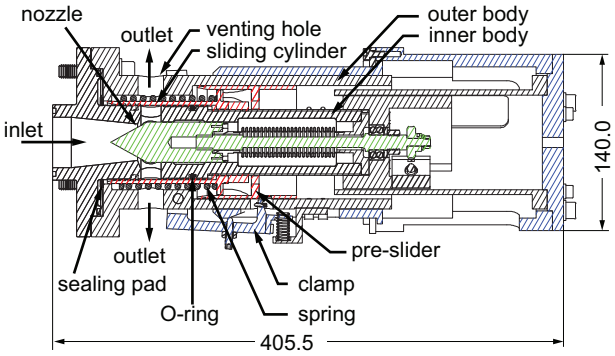

Figure 5: Drawing of the cross-section of the Fast Opening Valve. The actuation system (in blue) slides slowly to the right side, which pushes the clamps outward. Once the clamps release the pre-slider, the fast moving components (in red) come into motion because the compressed spring pushes the sliding cylinder and the pre-slider away. After the sliding cylinder is pushed across the venting holes, he fluid is free to flow from the inlet to the outlet. The nozzle insert (in green) can be moved in the longitudinal direction in order to control the throat area.

conductivity. This is required to obtain a uniform temperature and to prevent hot spots that could promote thermal decomposition. The entire vapour generator is covered with a layer of minimum 50 mm rockwool insulation to limit heat losses to the environment.

Once the desired pressure is attained in the vapour generator, a manually operated Tyco 19.05 mm globe valve MV-4 (type Megastar) is opened and vapour flows through pipe 4 to the reference tube (RT) and charge tube (CT), see Fig. 3. The purpose of the RT is to finely control the vapour superheating and to provide a reference for the thermal control of the CT, as further explained in Sec. 2.2. The RT is a 500 mm long tube with an internal diameter of 40 mm and 15 mm thick walls. The thickness of the walls enhances an even distribution of the thermal power. The thermal energy is supplied by two Tyco custom-made heating jackets around the tube, which includes a 25 mm glass silk insulation layer. A 335 W version is placed around the RT and a 180 W version around the flange of the RT. To prevent condensation in pipe 6, see Fig. 3, a 2.1 m long 370 W Welvy Joule dissipation heating wire (type HSQ/021) is applied with a 2 mm thick graphite layer placed underneath.

The geometry of the CT and of the RT are identical, except for their length. The CT is composed of six pipe segments, each 1520 mm long. The pipe segments feature a male-to-female connection and a red copper seal (see the zoomed section in Fig. 3) which allow for satisfactory sealing both in case the inner volume is at superatmospheric pressure, or under vacuum conditions. The CT assembly measures 9 m in total and is placed on a sliding support to allow for its thermal expansion when at high temperature. Each segment is fitted with a custom made Tyco 950 W Glass Silk heating jacket and the couplings between the elements are fitted with two 0.5m Welvy 180 W Joule heating electric wire (type: HBQ/005), all covered by a 25 mm glass silk insulation layer. Immersion of temperature sensors in the CT would inherently disturb the flow field of interest. Instead, the outside wall temperature is measured both in the RT and CT. Due to the geometric equivalence of the RT and the CT, imposing the same temperature on the walls results in the same fluid temperature inside the tube.

The end of the CT is closed off by a FOV, arguably the most complex mechanical part of the setup, see Fig. 5. This custom designed valve is able to operate at high temperatures without lubrication to

avoid contamination of the working fluid. It might however be expected that the siloxane working fluids act as a lubricant. The valve is contained in the LPP and can be operated remotely, keeping the entire facility hermetically sealed for multiple experiments. In the opened position, the working fluid can flow through venting holes present in the inner and outer body in the radial direction. In the closed position, a sliding cylinder is pushed between these bodies, obstructing the flow through the venting holes. The sliding cylinder presses into a Kalrez compound sealing pad on the flange to ensure sealing. On the other side, the sealing is performed by a Kalrez O-ring with a diameter of 47.22 mm and a thickness of 3.53 mm between the sliding cylinder and the inner body. Since the thermal swelling of the O-ring has a strong effect on the friction of the sliding cylinder during the fast opening, a 3 mm thermocouple (K-type) inserted in a hole in the mounting flange of the FOV monitors the temperature of the steel. An Inconel steel spring is compressed and three radial clamps engage the pre-slider to prevent the spring from being released. To open the valve, the clamps are moved in the outward direction, allowing the spring to push the sliding cylinder and the pre-slider away, thus leaving the venting holes open. A nozzle insert creates a throat area in order to choke the flow, thus preventing flow disturbances from travelling upstream. For this reason the throat is located upstream of the sealing, as opposite to solutions that are typical in Ludwieg tubes (Schrijer and Bannink, 2010; Knauss et al., 1999). The nozzle insert can be moved remotely in the longitudinal direction to change the throat area section, between approximately 420 mm^2 and 600 mm^2, and this allows to modulate the strength of the rarefaction waves.

The FOV is contained in the LPP, a 113 liter cylindrically shaped vessel, see Fig. 3, with an outer diameter of 406.4 mm and 9.53 mm thick walls. The electric motor triggering the FOV and the manual nozzle positioning gear are mounted on the LPP with feedthrough shaft connections sealed with copper gaskets. A lid gives access to the vessel interior for installation of the FOV, and is sealed by a graphite gasket. The LPP can be heated by 4 custom built Tyco heating jackets with a nominal power of 1450, 425, 960 and 490 W respectively.

The vapour flows from the LPP through globe valve PV-1 into a condenser. The condensed liquid accumulates in a flow return pipe and returns via globe valve PV-2 into the vapour generator, see Fig. 3.

2.2 Instruments & Control

The thermal energy supply to the various sections of the facility is regulated by digital PID controllers, which modulates the electrical voltage to the heating elements via RKC 1-phase thyristors (model: THV-1PZ-020-5*NN-6).

In the vapour generator, the static pressure had initially been used as process variable for the main heater at the bottom section, measured by a Klay pressure transmitter (type 2000-SAN-4-F(w)-I-HT-G43) with a specified accuracy of 0.1% of the full range of 30 bar. Because the operating pressure range of the vapour generator spans from very far from the critical point to close-to-critical conditions, the response in pressure to the supplied thermal power changes dramatically, due to the difference in the pressure derivative with respect to temperature at constant specific volume $\left(\frac{\partial P}{\partial T}\right)_v$. Consequently, the PID parameters should also be adapted depending on the operated pressure. This is avoided by converting the pressure into a saturation temperature with the help of in-house software (Colonna et al., 2012) implementing suitable fluid thermodynamic property models, (see, e.g. Nannan and Colonna 2009). Now the same PID parameters can be used throughout the entire operating range, because the change in specific heat capacity is sufficiently moderate. At the same time, the fast response of the pressure transmitter is still exploited for the control. The fluid saturation temperature is compared by a direct measurement of the liquid temperature as sensed by a Klay 4-wire Pt-100 sensor with insertion length of 180 mm and 6 mm diameter (type TT-E-D-F-L180xD6-S-P2-P13), which is calibrated using a Presys calibration oven (type T-350P) to within a tolerance of 0.12 °C. The other heaters on the vapour generator are each regulated based on the temperature difference as measured by the Pt-100 and a 1 mm thick thermocouple (K-type) applied underneath each heater.

The heat supply to the RT is regulated by a PID controller with as process variable the superheating of

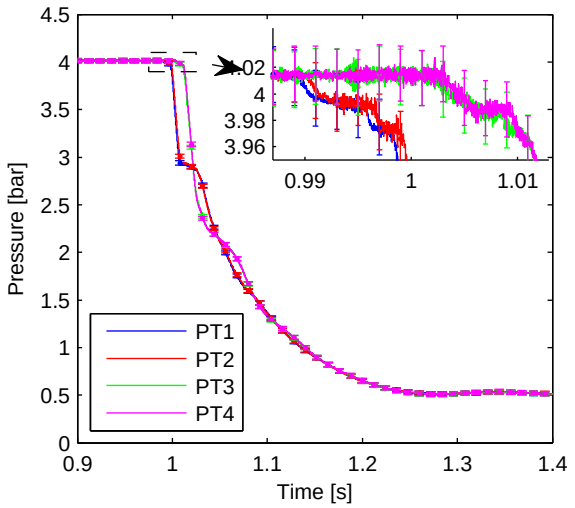

Figure 6: Pressure signals of experiment 25 measured by transducers PT1 to PT4. The valve opening results in a pressure drop from 3.97 bar to 2.88 bar, which is preceded by two other small pressure drops. These are attributed to an initial leakage flow that starts as soon as the FOV sliding cylinder detaches from the seal.

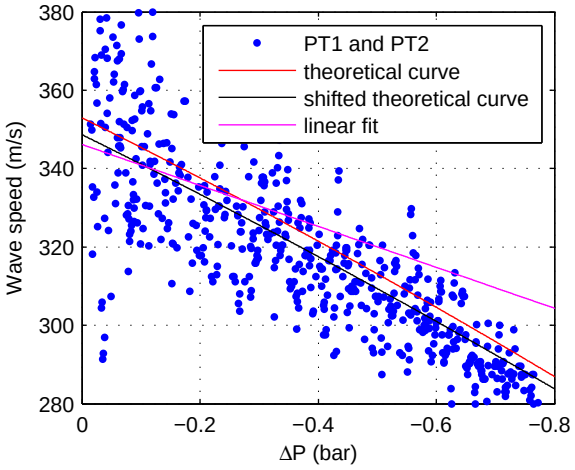

Figure 7: Wave Speed in N_2 as a function of the pressure drop. The blue dots are the experimental results obtained with the time-of-flight method. The red line is the theoretical curve. The black line is a shift of the theoretical curve with the average deviation from the theoretical curve. The magenta line is a linear fit of the data. The shifted theoretical curve and the linear fit are made based on 25 % of Δp_{rel} = -0.2 bar

the vapour, measured by the difference in temperature of the vapour in the RT and of the liquid in the vapour generator. The temperature in the RT is measured with a Klay 3-wire Pt-100 sensor (type TT-E-D-F-L250xD6-S-P2-P13) with 250 mm insertion length and 6 mm diameter, and is calibrated in the same manner as the one in the vapour generator. An identical resistance temperature detector (RTD) as the one in the RT is used to monitor the temperature in the CT.

The fluid temperature inside the CT is controlled by imposing the same wall temperature on the CT as on the RT, which are geometrically equivalent, except for the length. The process variable of each control loop is the difference in wall temperature between the RT and the respective CT pipe segment and coupling. Instead of measuring the temperature of the two thermocouples and calculating the difference in temperature, here the two thermocouples are connected to each other and the voltage difference is directly measured to reduce the measurement error. The 1 m long and 0.5 mm thick thermocouple (type K) is placed in a groove in the RT and in each CT element, bonded to the tube with Aremco silver-filled conductive ceramic adhesive (type 597A) to ensure the measurement of the wall temperature.

To measure the passing rarefaction, four dynamic pressure measurement stations PT1-PT4 are created by flush mounting a high-temperature Kulite fully active four arm wheatstone bridge pressure transducer (type XTEH-10LAC-190M-21bar-A) that measures the pressure with an accuracy of 0.5 % of the full scale of 21 bar along the CT at a distance of 4, 4.3, 8.4 and 8.7 m from the FOV respectively, see Fig. 3. The signals acquire at a frequency of 250 kHz and are scaled after each experiment with the more accurate value of the pressure before and after the experiment, measured by the static pressure transducers. The sensors are placed in pairs to give the possibility to have a time of flight measurement at two different locations in the tube.

nr	fluid	P_{CT} [bar]	T_{CT} [°C]	Γ [-]	ΔP_{wave} [bar]	A_{nozzle} [mm^2]	c_{model} [m/s]	c_{fit} [m/s]	c_{shift} [m/s]
1	He	6.01	17.3	1.34	1.74	459	1006	998	964
2	He	4.90	22.7	1.34	0.28	79	1014	1014	1028
3	He	6.09	48.9	1.34	1.69	438	1059	1005	1072
4	He	6.50	50.0	1.34	0.32	67	1060	1121	955
5	He	6.66	99.2	1.34	2.01	483	1138	1274	1169
6	He	6.02	149.4	1.34	1.84	489	1212	1225	1182
7	He	7.29	269.4	1.34	0.33	62	1373	1547	1348
8	He	8.47	269.9	1.34	0.44	72	1374	1424	1483
9	air	6.31	17.6	1.21	1.62	456	343	341	341
10	air	4.08	18.0	1.20	0.97	418	343	338	339
11	air	7.01	19.1	1.21	1.81	459	344	338	339
12	air	4.86	20.0	1.21	0.21	67	344	359	350
13	air	5.39	20.0	1.21	0.23	68	344	344	353
14	air	7.13	22.0	1.21	0.30	67	345	338	347
15	air	6.15	49.1	1.21	1.62	468	361	353	356
16	air	6.98	95.0	1.20	0.27	61	386	375	388
17	air	6.80	99.5	1.20	1.76	461	388	390	384
18	CO_2	5.99	18.0	1.13	1.50	471	262	257	259
19	CO_2	6.42	50.0	1.12	1.59	465	275	274	273
20	CO_2	6.64	100.3	1.12	1.64	464	296	294	293
21	CO_2	6.13	149.7	1.11	1.50	459	314	321	315
22	N_2	1.09	25.3	1.20	0.35	576	352	337	338
23	N_2	1.12	25.4	1.20	0.33	531	352	379	349
24	N_2	4.00	25.7	1.20	1.00	443	353	360	353
25	N_2	4.01	25.8	1.20	1.08	481	353	346	349
26	D_6	1.26	264.2	0.86	0.09	169	89.8	89.5	88.4
27	D_6	1.26	293.7	0.91	0.15	278	94.3	94.0	94.1
28	D_6	1.27	298.0	0.91	0.18	328	94.8	96.9	93.9
29	D_6	1.27	300.1	0.92	0.14	254	95.1	98.3	94.0
30	D_6	2.52	301.1	0.79	0.26	254	84.6	84.9	83.5
31	D_6	2.38	302.3	0.81	0.21	220	86.2	83.5	82.7
32	D_6	2.53	305.1	0.79	0.29	286	85.4	84.3	83.5

Table 1: Results from rarefaction measurements. p_{CT} and T_{CT} are the measured initial pressure and temperature in the charge tube. Γ and c_{model} are the fundamental derivative of gasdynamics and speed of sound respectively calculated using the most accurate thermodynamic model for the measured conditions (uncertainty unknown). Δp_{wave} is the pressure difference across the rarefaction. A_{nozzle} is the nozzle area calculated using the pressure drop across the expansion. c_{fit} and c_{shift} are the speed of sound as measured by fitting the experimental time-of-flight results using a linear function and by shifting the theoretical curve with the average deviation respectively.

3. RAREFACTION WAVES IN INCONDENSABLE GASES.

In order to verify the correct functioning of the facility, a series of experiments are performed using incondensable gases in the ideal gas regime. The CT is filled with the gas under pressure, while the LPP is kept at vacuum conditions. The FOV is opened after which a rarefaction wave propagates into the CT, see Fig. 2. A flow starts from the CT into the LPP, which is attaining a sonic speed in the throat.

The pressure recordings of rarefaction experiment 25 (see Table 1) are displayed in Fig. 6. The working fluid in that experiment is nitrogen and the pressure is 4.01 bar in the CT and < 10 mbar in the LPP, both at an ambient temperature of 25.8 °C. The FOV opening sequence can be inferred from these pressure data: as soon as the FOV opening is initiated, the sliding cylinder is pushed by the compressed spring, see Fig. 5. A small opening is created when the sliding cylinder does not touch the seal anymore, and the flow gets choked close to this position. This causes a small pressure drop of approximately 20 mbar. As the slider moves further, the position of minimum cross-section of the flow changes to a section between the slider and the inner body, which is slightly larger than the initial choked section. This is revealed by

a second small drop in the pressure of approximately 20 mbar. Finally the sliding cylinder passes over the venting hole of the inner body, and the flow chokes at the designated nozzle. This is seen as the large pressure drop down to 2.88 bar.

The nozzle throat cross-sectional area is not easily recovered from the FOV geometry and therefore it is inferred from the measurements by assuming a steady flow from state B through the nozzle, see Fig. 2. The mass flow in state B is evaluated using the density calculated by using the isentropic relations from state A, the known cross-sectional area of the CT and the evaluated flow velocity using the Riemann invariant from state A. The isentropic relations are used to calculate the density and velocity in the throat. The calculated throat area ranges from 418 to 576 mm^2. Several experiments were performed using a special nozzle insert, for which the calculated throat area ranges from 61 to 79 mm^2, see Table 1.

The local wave propagation speed in the CT equals the local speed of sound minus the local flow velocity. A theoretical curve can be constructed by calculating the wave propagation speed as a function of the pressure drop of the rarefaction. At zero pressure drop, the wave propagation speed equals the speed of sound, since stagnant conditions are assumed in the CT before opening the valve, and is evaluated using the reference equation of state. For a given pressure drop, the wave propagation speed is evaluated by calculating the local speed of sound using the isentropic relations, while the local flow velocity is calculated by evaluating the Riemann invariant in the undisturbed state (Thompson, 1988).

By applying the time-of-flight method to the signals of two pressure transducers, an experimental value of the local wave propagation speed is obtained. This is done by first selecting the relevant part of the pressure signal as follows: the beginning of the wave at $t = t_{start}$ is formally identified as the time when the pressure departs more than 15 mbar from the initial value P_{CT}. The threshold is chosen such that it exceeds the noise level. The end of the unperturbed portion of the signal is chosen when the head of the wave is expected to reach the end of the CT at $t = t_{end}$. The estimate is performed by using the speed of sound from the accurate reference thermodynamic model, therefore $t_{end} = t_{start} + \Delta x / c_{model}$, where Δx is the distance between the sensor location and the end of the CT. The relevant portion of the signal ΔP_{rel} spans from P_{start} to P_{end}. This span is divided into intervals of two times the resolution of 0.32 mbar of the pressure signal of the current measurement system. The time-of-flight method is applied to corresponding subintervals from different sensors to compute the local wave propagation speed. The measurements of sensors PT3 / PT4 are quickly influenced by the reflection of the rarefaction from the CT end wall, so only the measurements of sensors PT1 / PT2 are considered.

Fig. 7 shows for the example of experiment 25 the charts that can be obtained, from which the speed of sound can be retrieved at $\Delta p \to 0$. Wave speed values as a function of the measured pressure drop are shown together with fitting curves used to estimate the speed of sound. To reduce inaccuracies introduced by the FOV in the determination of the speed of sound to a negligible level, only the first 25 % of the relevant pressure span is taken, while keeping a minimum of 40 mbar, such that $\Delta p_{max} = \max(0.25 p_{rel}, 0.04\ bar)$. Two methods are used to fit the experimental data: a simple linear fit and a fit obtained by shifting the theoretical curve with the average deviation of the measurement points with respect to this curve. The resulting speed of sound c_{fit} and c_{shift} are reported in table 1. For air, CO_2 and N_2, both methods deliver an accurate estimate of the speed of sound, compared to the value obtained from the reference thermodynamic model (Lemmon et al., 2013), which corresponds to the ideal gas model in this regime. The only exception is the linear fit for experiment 23. The average error and standard deviation with respect to the model are 2.1 ± 1.6 % and 1.1 ± 1.1 % for the linear fit and the shifted theoretical curve respectively. For helium, the average error and standard deviation with respect to the model are 5.1 ± 4.6 % and 4.0 ± 3.1 % for the linear fit and the shifted theoretical curve respectively. The reason for the larger error is due to the higher speed of sound of helium in combination with the finite process start-up time of the FOV resulting in a very small usable relevant portion of the signal.

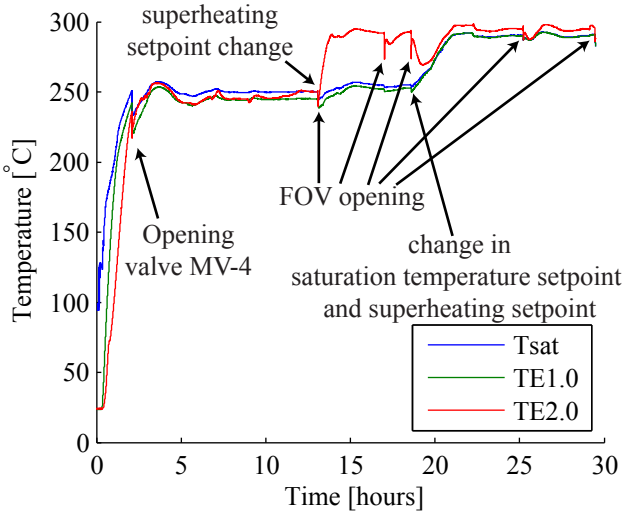

Figure 8: Temperature recordings during the experimental campaign on siloxane D_6. Tsat is obtained from the measured pressure in the vapour generator by means of the suitable thermodynamic model from Nannan and Colonna (2009). TE1.0 is the temperature measured by the PT-100 sensor in the vapour generator. TE2.0 is the temperature measured by the PT-100 sensor in the reference tube.

4. RAREFACTION WAVES IN SILOXANE D_6

Experiments to measure the expansion wave speed in D_6 (dodecamethylcyclohexasiloxane, $C_{12}H_{36}O_6Si_6$) are performed from which the speed of sound is estimated. Gaschromatographic analysis confirmed the specification of the supplier that the fluid has a 96 % purity. Experiments were conducted at several thermodynamic states, see experiments 26 to 32 in Table. 1. Fig. 8 shows the temperature of the fluid in the vapour generator and in the reference tube during the entire test campaign. Part of the liquid in the vapour generator is flashed each time valve MV-4 is opened after an experiment. The measured temperature fluctuations in the reference tube and charge tube had a period of approximately 2 hours with an amplitude of up to 3 °C for both temperature levels.

Pressure recordings of experiment 28 are displayed in Fig. 9. Calculations using the resulting pressure drop from the experiments result in a significantly lower nozzle area than the 460 to 600 mm^2 that was expected based on the geometry, see Table 1, which may indicate that there is accumulation of condensed fluid in the unheated FOV.

The wave propagation speed has been computed from the experimental data and compared with the theoretical curve, which is constructed in the same manner as for the incondensable gases. The ideal gas model can not be used in this case, and consequently the Riemann invariant can not be integrated analytically. The local flow velocity is instead evaluated by integrating the Riemann invariant numerically. Estimation of the speed of sound is obtained with the best available thermodynamic model for pure D_6, which shows a 30 % deviation on the speed of sound with the sole reliable measurement, which is performed in the liquid state (Colonna et al., 2008b). Results from experiment 28 are displayed in Fig. 10. The wave speed calculated from experimental data for this experiment is within 8 % of the value predicted by the thermodynamic model. Only for a pressure drop lower than 12 mbar the deviation is higher, because the pressure gradient is very low, thus the influence of noise more significant. By fitting the experimental data in the same manner as illustrated for the case of incondensable gases, i.e. using a linear fit, and by shifting the theoretical curve, the speed of sound c_{fit} and c_{shift} is obtained. The average error and standard deviation with respect to the value predicted by the thermodynamic model are 1.6 ± 1.2 % for the linear fit and 1.6 ± 1.1 % for the shifted theoretical curve. The experimental results are unexpectedly close to model predictions, considering that, differently from the case of incondensable

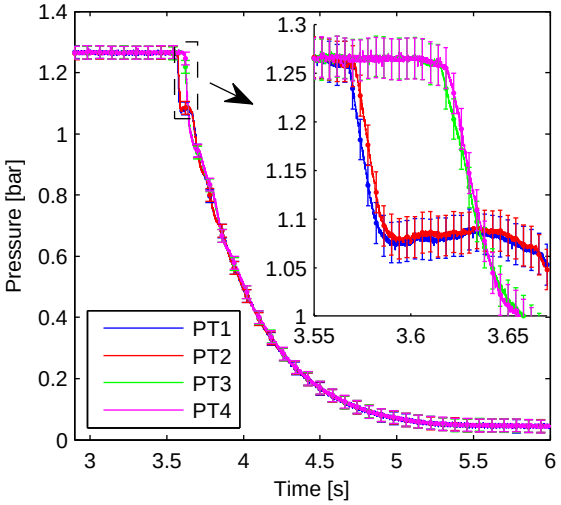

Figure 9: Pressure recordings during a D_6 experiment. The conditions in the CT are 1.27 bar and 298 °C. PT1 to PT4 are the pressure recordings of the sensor closest to the FOV to furthest away from the FOV, respectively.

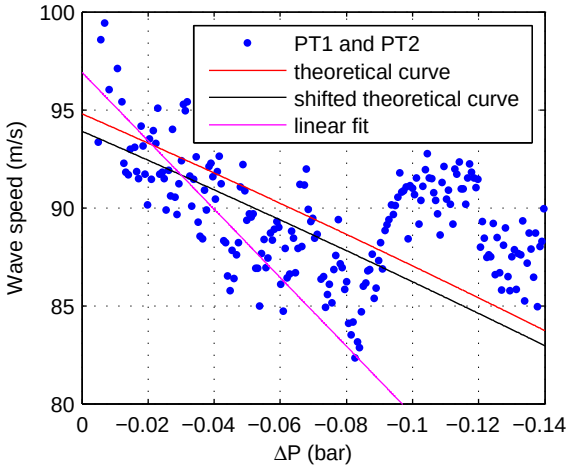

Figure 10: Wave speed in D_6 siloxane as a function of the pressure drop. The blue dots are the experimental results obtained with the time-of-flight measurements. The red line is the theoretical curve. The black line is a fit of the experimental data using a shift of the theoretical curve. The magenta line is a linear fit of the data.

gas, the D_6 thermodynamic model is expected to be rather inaccurate for states in the close proximity of the saturation curve.

5. CONCLUSION & FUTURE WORK

A novel Ludwieg-tube-type facility has been commissioned at Delft University of Technology, with the purpose of performing measurements on rarefaction waves in dense organic vapours. The pressure and temperature of the working fluid can be regulated independently from each other, such that any thermodynamic state can be achieved within the limits of the measurement system of 21 bar and 400 °C. Experiments on rarefaction waves in a number of incondensable gases have been conducted to validate the correct functioning of the facility. A novel algorithm is devised to estimate the speed of sound from rarefaction experiments. Experiments using siloxane D_6 show the feasibility of the original design concept up to 300 °C: rarefaction wave speed measurements were successfully performed, providing values of the speed of sound that are within 1.6% of the predictions of the best available thermodynamic model (the model itself is known to be affected by uncertainties of 30 % for the speed of sound).

REFERENCES

Brown, B. and Argrow, B. (2000). Application of Bethe-Zel'dovich-Thompson fluids in organic Rankine cycle engines. *J. Propul. Power*, 16(6):1118--1124.

Colonna, P., Casati, E., Trapp, C., Mathijssen, T., Larjola, J., Turunen-Saaresti, T., and Uusitalo, A. (2015). Organic Rankine cycle power systems: Fom the concept to current technology, applications and an outlook to the future. *J. Eng. Gas Turb. Power*, 137(10):100801.

Colonna, P., Guardone, A., Nannan, N., and Zamfirescu, C. (2008a). Design of the dense gas flexible asymmetric shock tube. *J. Fluids Eng.*, 130(3). 034501.

Colonna, P., Nannan, N. R., and Guardone, A. (2008b). Multiparameter equations of state for siloxanes:

$[(CH_3)_3\text{-Si-}O_{1/2}]_2\text{-}[O\text{-Si-}(CH_3)_2]_{i=1,\ldots,3}$ and $[O\text{-Si-}(CH_3)_2]_6$. *Fluid Phase Equilib.*, 263(2):115--130.

Colonna, P., van der Stelt, T. P., and Guardone, A. (2012). FluidProp (Version 3.0): A program for the estimation of thermophysical properties of fluids.

Conboy, T., Wright, S., Pasch, J., Fleming, D., Rochau, G., and Fuller, R. (2012). Performance characteristics of an operating supercritical CO_2 Brayton cycle. *J. Eng. Gas Turb. Power*, 134(11).

Cramer, M. S. (1989). Shock splitting in single-phase gases. *J. Fluid Mech.*, 199:281--296.

Dvornic, P. R. (2004). High temperature stability of polysiloxanes. *Silicon Compounds: Silanes and Silicones, Gelest Catalog*, pages 419--432.

Knauss, H., Riedel, R., and Wagner, S. (1999). The shock wind tunnel of Stuttgart university - a facility for testing hypersonic vehicles. In *9th International Space Planes and Hypersonic Systems and Technologies Conference*, number AIAA 99-4959.

Lemmon, E., Huber, M., and McLinden, M. (2013.). NIST standard reference database 23: Reference fluid thermodynamic and transport properties-REFPROP, version 9.1.

Nannan, N. and Colonna, P. (2009). Improvement on multiparameter equations of state for dimethylsiloxanes by adopting more accurate ideal-gas isobaric heat capacities: Supplementary to P. Colonna, N. R. Nannan, A. Guardone, E. W. Lemmon, Fluid Phase Equilib. 244, 193 (2006). *Fluid Phase Equilib.*, 280(1--2):151--152.

Nannan, N., Colonna, P., Tracy, C., Rowley, R., and Hurly, J. (2007). Ideal-gas heat capacities of dimethylsiloxanes from speed-of-sound measurements and ab initio calculations. *Fluid Phase Equilib.*, 257(1):102--113.

Rinaldi, E., Pecnik, R., and Colonna, P. (2015). Computational fluid dynamic simulation of a supercritical CO_2 compressor performance map. *J. Eng. Gas Turb. Power*, 137(7):072602.

Schrijer, F. and Bannink, W. (2010). Description and flow assessment of the delft hypersonic ludwieg tube. *J. Spacecraft Rockets*, 47(1):125--133.

Thompson, P. A. (1971). A fundamental derivative in gasdynamics. *Phys. Fluids*, 14(9):1843--1849.

Thompson, P. A. (1988). *Compressible Fluid Dynamics*. McGraw-Hill.

Weith, T., Heberle, F., Preißinger, M., and Brüggeman, D. (2014). Performance of siloxanes mixtures in a high-temperature organic Rankine cycle considering the heat transfer characteristics during evaporation. *Energies*, 7:5548--5565.

Zamfirescu, C. and Dincer, I. (2009). Performance investigation of high-temperature heat pumps with various BZT working fluids. *Thermochim. Acta*, 488(1–2):66 -- 77.

ACKNOWLEDGEMENT

This research is partly funded by Dutch Technology Foundation STW, the Technology Program of the Ministry of Economic Affairs (DSF 11143) and by the European Research Council under grant ERC Consolidator 2013 (NShock 617603)